Unveiling the power of titanium dioxide for energy storage and electrochemical technologies

ChemCatChem

Research Article
doi.org/10.1002/cctc.202401689

Chemistry Europe
European Chemical Societies Publishing

www.chemcatchem.org

Unveiling the Power of Titanium Dioxide for Energy Storage and Electrochemical Technologies

Luisa Baudino,[a, b] Pietro Zaccagnini,[a, b] Stefano Bianco,[a] Micaela Castellino,[a, b] Andrea Lamberti,*[a, b] C. Fabrizio Pirri,[a, b] and Mara Serrapede[a, b]

Titanium dioxide nanotubes (TiO_2 NTs) have been widely investigated in the past 20 years due to a variety of possible applications of this material. Indeed, their high surface area and tunable morphology can easily implement key features of TiO_2, such as its biocompatibility and photo- and electrocatalytic properties. This combination makes TiO_2 NTs perfect candidates for multifunctional applications ranging from biomedical application to sensing and energy devices. Herein, we present TiO_2 NTs grown by anodic oxidation on top of a titanium foil in an ethylene glycol-based electrolyte with NH_4F. The as-grown amorphous nanotubes were then subjected to annealing in a reducing atmosphere at different temperatures while maintaining their amorphicity. The morphological, physicochemical, and electronic properties were then thoroughly evaluated to assess their use in different fields, from energy storage devices to photo-catalytical applications.

1. Introduction

Titanium is the ninth most abundant element on Earth. Its oxide, titania, possesses unique properties such as heat and corrosion resistance, and it is lightweight with exceptional mechanical properties. Its increasing demand in several industries, and the limited availability, have led the community to consider it a critical raw material.[1] However, the development of extraction technologies and recycling methodologies will ensure a sustainable and continuous supply in the future.

Among all its applications, titanium dioxide, that is, titania, spans the energy sector, especially in alkali metal batteries, but has also been used in supercapacitors, fuel cells, and dye-sensitized solar cells.[2–11] In particular, this material presents remarkable performances in Li-ion battery (LIB) systems as an anode material since the low volume change upon the reversible Li-ion insertion and extraction does not cause any structural instability.[12–15] However, titanium dioxide is also widely used in different applications such as sunscreen, paints, and photocatalysis due to its excellent optical and photocatalytic properties.[16–19]

Among the several different nanostructures of titania available, self-organized titania nanotubes (TiO_2 NTs) are generally considered the most versatile.[11,20–30] In fact, when prepared by anodic oxidation on top of a metallic foil, the NTs can be either used with the in-built current collector or detached from it. Similarly, while the anodic oxidation synthesis provides amorphous nanotubes, depending on the temperature of the successive annealing the NTs can be converted in one of their crystalline phases, most notably anatase or rutile. Instead, depending on the atmosphere of the annealing temperature, oxygen vacancies (OVs) or doping atoms can be introduced into their structure to boost their electronic properties.[31–33] Furthermore, as is well-known in the field of energy storage devices, creating vacancies in oxide phases and making them amorphous shifts the storage mechanism far from diffusion-controlled mechanisms and towards surface-controlled ones leading to a prevalent capacitive-like behavior.[34]

The term "black titania" usually denotes TiO_2 that has been engineered to have unique properties, that is, modified to adsorb a broader spectrum of light, including visible and infrared wavelengths. This modification is often achieved through doping or surface treatments, which alter the electronic structure of the material. The enhanced light absorption of black titania makes it potentially useful for applications such as solar energy conversion and photothermal therapy.[35–41]

In electrochemical applications, black titania may be used as an electrode material in devices such as lithium-ion batteries, supercapacitors, and photoelectrochemical cells. The electrochemical properties of black titania nanoparticles can vary depending on factors such as their size, morphology, surface chemistry, and any doping or modifications that have been made to the material. The electrochemical stability of black titania refers to its ability to withstand the electrochemical reactions occurring at its surface without undergoing degradation. Enhanced stability is crucial for long-term device performances. The rate at which the charge is transferred between

[a] Dr. L. Baudino, Dr. P. Zaccagnini, Prof. S. Bianco, Dr. M. Castellino, Prof. A. Lamberti, Prof. C. F. Pirri, Dr. M. Serrapede
Department of Applied Sciences and Technology–DISAT, Politecnico di Torino, Corso Duca degli Abruzzi 24, Torino 10129, Italy
E-mail: andrea.lamberti@polito.it

[b] Dr. L. Baudino, Dr. P. Zaccagnini, Dr. M. Castellino, Prof. A. Lamberti, Prof. C. F. Pirri, Dr. M. Serrapede
Center for Sustainable Future Technologies, Istituto Italiano di Tecnologia, Via Livorno 60, Torino 10144, Italy

Supporting information for this article is available on the WWW under https://doi.org/10.1002/10.1002/cctc.202401689

the electrode surface and the electrolyte solution is critical for the performance of electrochemical devices. Surface modifications or doping of black titania nanoparticles can influence charge transfer kinetics.[42,43] Moreover, these nanoparticles may exhibit electrocatalytic activity, catalyzing specific electrochemical reactions, such as oxygen reduction or evolution reactions in fuel cells, or water-splitting reactions in photoelectrochemical cells.[44–53]

Black TiO_2 nanotubes produced via anodic oxidation and then annealed under a reducing atmosphere are a fascinating area of research with potential applications in various fields due to their unique properties. The nanotubular structure provides a large surface area, which is advantageous for applications such as catalysis, sensing, and energy storage,[33,54–56] and when working with amorphous NTs it is possible to use lower annealing temperatures, thus reducing the impact of the process.[45] Black TiO_2 nanotubes exhibit enhanced light absorption and a reduced bandgap compared to their conventional counterparts. This improved light absorption extends into the visible and near-infrared regions of the spectrum, making them potentially useful for photocatalysis and photovoltaic applications, but also environmental remediation, water purification, and solar fuel production.[57–60]

In the following study, amorphous TiO_2 nanotubes were prepared by anodic oxidation and successfully annealed under a reducing atmosphere to convert them into amorphous black TiO_2 nanotubes. Morphological, physicochemical, and electrochemical characterizations were then performed to assess their properties and to determine the best synthesis conditions for electrochemical applications.

2. Results and Discussion

Amorphous TiO_2 nanotubes were grown on titanium foil via a two-step anodic oxidation process in ethylene glycol (EG) electrolyte, and successively annealed in a reducing atmosphere at different temperatures.[61,62] Morphological characterizations were performed on the as-grown nanotubes and on the annealed samples to verify whether the thermal treatment influenced their morphology. As can be seen in the four panels of Figure 1, the nanotubes presented smooth walls and a length of approximately 5 μm after anodic oxidation (Figure 1a) and underwent no significant morphological changes when annealed at 150 °C (Figure 1b), 200 °C (Figure 1c) and 250 °C (Figure 1d).

X-Ray Diffraction (XRD) and Raman measurements were performed to confirm whether the samples had maintained their amorphous nature after the annealing step under reducing atmosphere. The thermal reduction treatment was performed at temperatures lower than 300 °C to avoid the formation of any crystallites.[63] As can be seen in Figure 2a all three samples annealed at 150 °C, 200 °C, and 250 °C presented no crystallographic peaks attributable to either anatase or rutile phase, indicated in the diffractograms as TiO_2 A and TiO_2 R, respectively. All the peaks that were recorded in the diffractogram were ascribed to the titanium foil substrate underneath the nanotube arrays.

Table 1. Breakdown of the different chemical states of the titanium and oxide components of the XPS HR spectra.

Sample	Ti^{4+}	Ti^{3+}	Ti^{0}	O^{2-}, Lattice Oxide	OH^{-}, Defective Oxides
As-grown	88.14%	7.76%	4.10%	64.74%	35.26%
150 °C	86.38%	8.30%	5.32%	75.33%	24.67%
200 °C	90.55%	6.55%	2.90%	75.14%	24.86%
250 °C	90.14%	5.63%	4.14%	83.62%	16.38%

The amorphous nature of the samples was further confirmed by Raman spectroscopy. As can be seen in Figure 2b, all the samples annealed show no active Raman bands under 1000 cm^{-1}. No signs of the anatase active modes of the B_{1g} band at ~400 cm^{-1}, $A_{1g} + B_{1g}$ at ~520 cm^{-1} or E_g band at ~640 cm^{-1} are visible.[51,64] Very broad bands appear at ~420 cm^{-1} and ~600 cm^{-1} in some of the annealed samples. While these could at first seem compatible to the E_g and A_{2g} bands in rutile,[65,66] there are no indications from the XRD diffractograms that there is any crystalline rutile in it, which at low temperatures requires severe conditions that are not met in the current study, including acidic media, long reducing treatments, and high pressures.[36,67] However, other studies have reported the presence of very broad bands at around ~420 cm^{-1} and ~600 cm^{-1} in amorphous samples and suggested that their presence could be motivated by the presence of increased oxygen deficiency at the surface, zone-edge disorders after hydrogenation, and even short range ordered rutile phase.[46,49,55,64,68–70]

Finally, to better understand the chemical states of the annealed nanotubes, X-ray photoelectron spectroscopy (XPS) analyses were performed on all samples. At first, a survey scan of all the samples confirmed the presence of only titanium and oxygen and of carbonaceous and fluoride impurities due to the anodic oxidation growth process of the nanotubes. However, it is worth mentioning that the fluoride contamination decreases after the thermal annealing (see Table S1 in the Supporting Information). High Resolution (HR) spectra of the main elements were then acquired to analyze their binding state. The HR Spectra of the Ti 2p and O 1s regions of the as-grown and 250 °C samples are reported in Figure 3. The complete survey scans, Ti 2p and O 1s HR spectra of all the samples, and details of peaks positions, are reported in the Supporting Information, respectively, as Figures S1–S3 and Table S2.

As can be seen from the two peaks centered at 458.8 eV ($Ti2p_{3/2}$) and 464.5 eV ($Ti2p_{1/2}$), the titanium presents itself mainly in the Ti^{4+} state bonded to oxygen atoms, drawn in blue in Figure 3a,b. Ti^{3+} states (indexed in green in Figure 3a,b), which should arise after the reducing annealing, are minoritarian with respect to the Ti^{4+} states. However, their superficial contribution seems to decrease after the thermal annealing in reducing atmosphere (except for the sample annealed at 150 °C, see Table 1). This could be partially due to their high reactivity at ambient atmosphere which could easily re-oxidize them into the Ti^{4+} state, a fact that could be enhanced by the disordered surface of the amorphous samples, or by the fact that increasing the temperature of the reducing treatment the Ti^{3+} states can

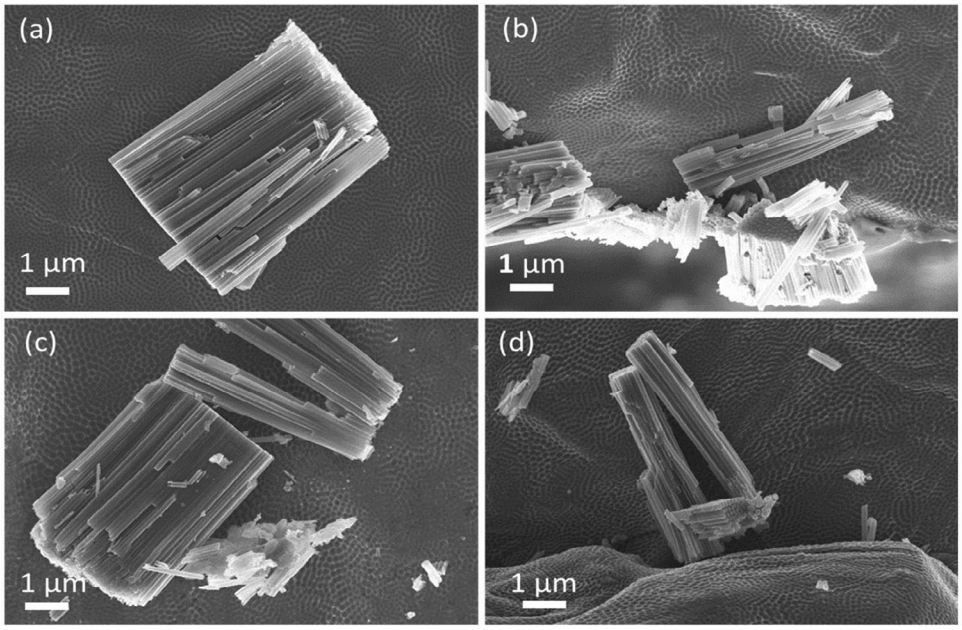

Figure 1. Micrographs of the TiO_2 nanotubes (a) as-grown and annealed at (b) 150 °C, (c) 200 °C, and (d) 250 °C.

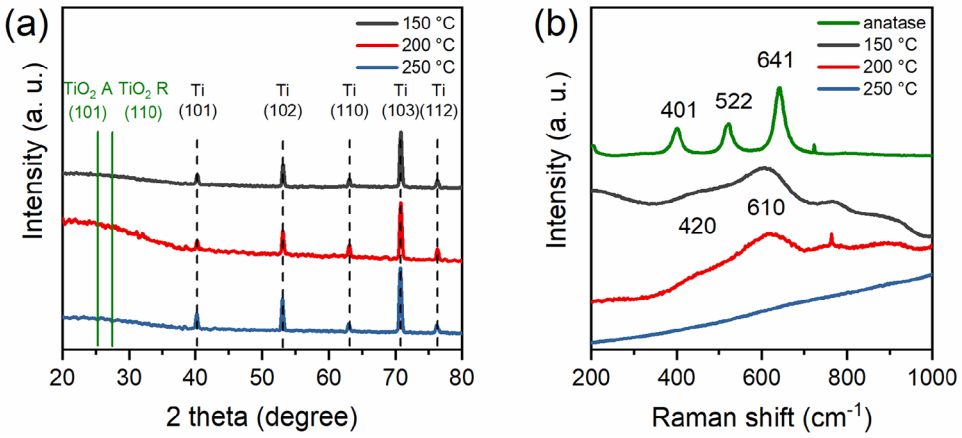

Figure 2. (a) Diffractograms of the samples annealed at 150 °C (black), 200 °C (red), and 250 °C (blue). The main peaks of the titanium substrate (Ti) have been indexed as the peaks of the crystalline phases anatase (TiO_2 A, in green) and rutile (TiO_2 R, in green) which are absent in all the annealed samples. (b) Raman spectra of the analyzed samples. A reference sample of anatase is displayed in green, whereas the samples annealed at 150 °C, 200 °C, and 250 °C are displayed in black, red, and blue, respectively.

diffuse deeper in the sample and thus result less visible through XPS measurements in analogy with rutile samples.[36]

The literature reports discord information on the presence and visibility of Ti^{3+} states in black titania samples. While some studies report their presence as fundamental in determining the samples properties,[47,71,72] others did not notice any change in the chemical environment of titanium atoms after the reducing annealing treatment.[11,36,64,73–75]

The O 1s HR spectra are shown to be asymmetrical and could be deconvoluted into two components (see Figure 3c,d). The first peak, at about 530 eV, represents the TiO_2 bonds of the lattice oxide while the second between 531 eV and 532 eV represents the Ti—(OH) bonds, a common feature in amorphous samples grown by anodic oxidation[20,76] and superficial defects caused by a partial reduction of titanium atoms.[47,49,50,57] Similarly to what happens with Ti^{3+} states, contrasting information can be found in the literature about whether the amount of hydroxyl groups found in the black titania samples should increase or decrease after the hydrogenation treatment.[43,47,48] The samples here analyzed showed that the amount of superficial defective oxides decreased after the thermal annealing in reducing atmosphere with respect to the samples as grown (see Table 1). This could mean that after the reducing thermal annealing our samples are less disordered while conserving their amorphous nature, or that the amount of surface hydroxyl groups deriving from the anodic oxidation synthesis was reduced and only the ones from the reducing treatment are still present.

Diffuse reflectance UV–VIS measurements were performed to determine the band gap of the treated samples, since reduction treatments and hydrogenation are known to lower the band

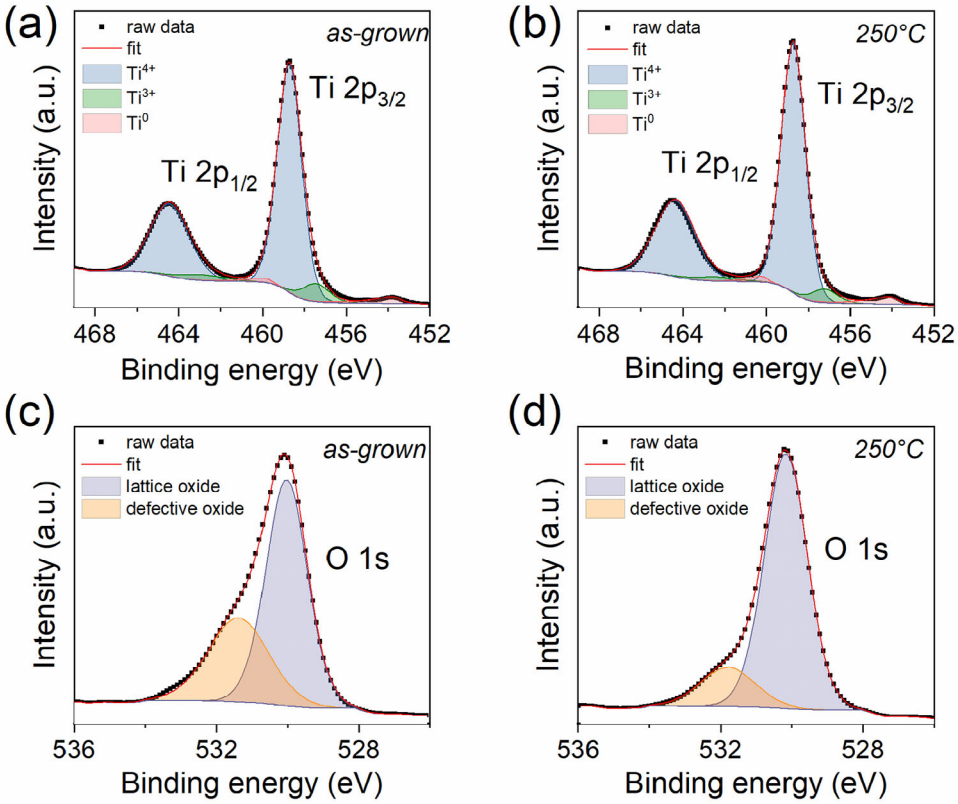

Figure 3. High Resolution spectra of the Ti 2p peaks of (a) as-grown nanotubes and (b) nanotubes annealed at 250 °C. Ti^{4+} states are depicted in blue, Ti^{3+} states in green and Ti^{0} in pink. High Resolution spectra of O 1s peaks of (c) as-grown nanotubes and (d) nanotubes annealed at 250 °C. The lattice oxide component is shown in purple while the defective oxide component in orange.

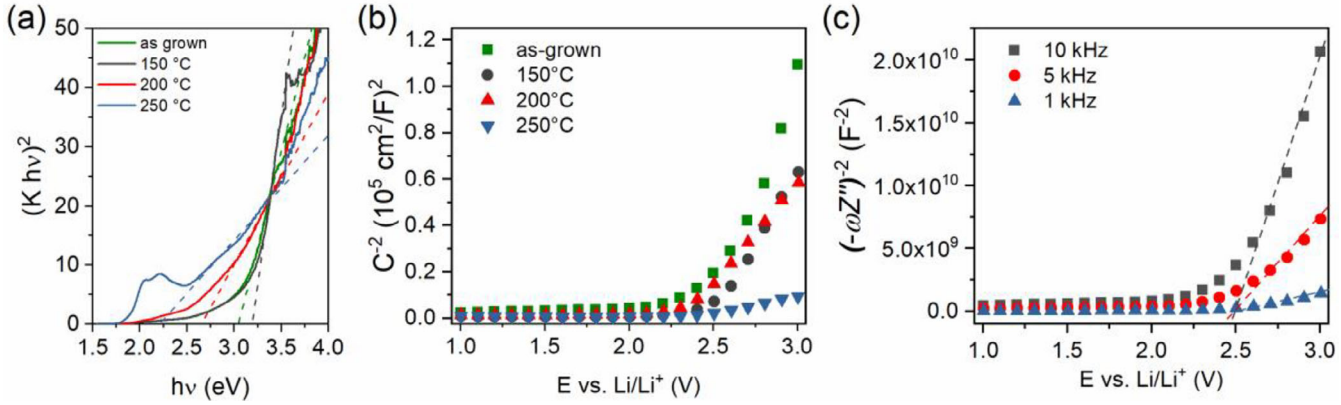

Figure 4. (a) Tauc plots of the samples annealed at different temperatures. As-grown amorphous NTs are displayed in green, whereas the samples annealed at 150 °C, 200 °C, and 250 °C are displayed in black, red, and blue, respectively. (b) Comparison of the Mott–Schottky curves of the four samples at 10 kHz. (c) Mott–Schottky curves at different frequencies of the as-grown nanotubes sample. The donor density was estimated from the slope the curves acquired at 10 kHz, while the flat band potential from the intersection of the curves acquired at different frequencies. Black squares indicate the data acquired at 10 kHz, red circles the ones at 5 kHz, blue triangles the ones at 1 kHz.

gap of titania.[47,77] According to different studies, from both an experimental and modeling point of view, amorphous TiO_2 should have a band gap higher than 3 eV independently from it being direct or indirect.[20,47,69,78–80] Although studies generally agree with white titania showing a preference for indirect band gap, black titania has been shown to present a direct band gap, regardless of it being amorphous or crystalline, and this was the case of our samples.[43,46,47,81] Tauc plots were drawn for all samples (see Figure 4a) following the Kubelka–Munk Equation (1) for direct configuration:

$$(K \times h\nu)^{(1/n)} = A\left(E_g - h\nu\right) \quad (1)$$

where K is the Kubelka-Munk function given by Equation (2):

$$K = \frac{\left(1 - R'_\infty\right)^2}{2R'_\infty} \quad (2)$$

Table 2. Electronic and electrochemical properties of the as-grown and black TiO_2 NTs. The values of indirect and direct band gap were obtained from the linear interpolation of the Tauc plots, the maximum of the valence band with respect to the Fermi level from XPS measurements. The carrier density N_D and flat band potential were computed from Mott–Schottky measurements, while the capacitive-controlled contribution to charge storage at 1 mV s^{-1} (called %C-control) and areal capacitances C_S were computed from cyclic voltammetry measurements.

Sample	Direct Band Gap (eV)	VB_{max} (w.r.t. Fermi Level, eV)	N_D (cm^{-3})	Flat Band Potential (eV)	%C-Control (at 1 mV s^{-1})	C_S (at 0.2 mV s^{-1}, mF cm^{-2})
As-grown	3.05	2.70	$4.68*10^{19}$	2.50	63	236.80
150 °C	3.20	2.58	$7.46*10^{19}$	2.50	71	267.40
200 °C	2.65	2.69	$1.08*10^{20}$	2.34	74	388.30
250 °C	2.20	2.65	$5.87*10^{20}$	2.40	80	398.37

where R'_∞ is the reflectance data from the diffuse reflectance spectroscopy measurements, A is a constant, $h\nu$ the energy of the photon, E_g the band gap of the sample,N_D and n is equal to 2 in the case of indirect gap and $\frac{1}{2}$ in the case of direct band gap.

Coherently with what previously reported for black titania samples and as can be seen in Figure 4a, our amorphous samples present a direct band gap of around 3 V while the annealed samples present lower values. For the sake of completeness an indirect band gap configuration was also considered, and the Tauc plots which were non-conclusive are reported in the Supporting Information as Figure S4. The values obtained for the different samples are reported in Table 2 together with the valence bands maxima with respect to the Fermi level evaluated from the XPS spectra. The values herein found are significantly lower than those reported in literature for black amorphous samples.[47] It can be seen that the band gap is indeed smaller when reducing the nanotubes, except for the sample annealed at 150 °C which shows a slightly higher value, similarly to what was observed in the Ti^{3+} states obtained from XPS analyses.

The density of donors N_D and flat band potentials were computed from Mott-Schottky measurements, that is, electrochemical impedance spectroscopy (EIS) measurements performed in the same lithium-based organic electrolyte and potential window of the electrochemical measurements. As can be seen in Figure 4b,c, the positive slope confirms that the black amorphous titania nanotubes are *n*-type electrodes. By assuming a value of dielectric constant ε equal to 15, averaging the values found in literature for amorphous TiO_2 samples,[82,83] the donor density N_D was computed according to Equation (3):

$$\frac{d\left(C^{-2}\right)}{dV} = \frac{2}{qA^2\varepsilon N_D\,(w)} \tag{3}$$

where A is the surface, q is the elemental charge, and $\frac{d(C^{-2})}{dV}$ is the above-mentioned slope. The flat band potentials were estimated from the intercept of each set of curves at three different frequencies, 10 kHz, 5 kHz, and 1 kHz, and are listed with the estimated donor densities in Table 2. The details of this procedure for the as-grown nanotubes are reported in Figure 4c, while the complete set for all samples is reported in the Supporting Information as Figure S5. As can be seen from the values reported in Table 2, the impedance spectroscopy measurements confirmed the lowering of the flat band potential, and that the annealing at higher temperatures resulted in an increase of the donor density of more than one order of magnitude.

Electrochemical characterizations were performed in lithium-based organic electrolyte to evaluate the kinetic effects induced by the different annealing processes. As it is possible to observe from Figure 5a, the cyclic voltammograms (CV) expressed in terms of differential capacitance and recorded on the four samples manifest no substantial differences in terms of shape, as they all show broad redox peaks, a further signature of their amorphous structure. It is possible to see that the as-grown nanotubes present an anodic shoulder at around 1 V, which is absent in the annealed samples. This shoulder can be attributed to irreversible reactions due to traces of water trapped in the tubes, which are no longer present in the annealed samples.[84–86] It is worth mentioning that, while everything is electrochemically reversible, both the position and the separation between the reduction and oxidation peaks increase as the annealing temperature increases, with a more notable effect during the oxidation process.

A kinetic analysis based on Dunn's method[87] allowed to determine the predominant mechanism of charge storage, and thus to quantify the amount of charge stored through fast capacitive mechanism, according to Equation (4):

$$i\,(V) = k_1\ \nu + k_2\ \sqrt{\nu} \tag{4}$$

where ν is the scan rate, and k_1 and k_2 are the kinetic constants responsible for the surface capacitive controlled and diffusion-controlled components, respectively. A graphical representation of the capacitively controlled current contribution I_{cap} for the electrode treated at 250 °C is shown in Figure 5b, where it is depicted with a dashed light blue line versus the total current I_{tot} indicated with a solid dark blue line. The capacitive-controlled percentages of each electrode are reported together with their areal capacities C_S at 0.2 mV s^{-1} in Table 2.

According to the coulombic efficiency and areal capacitances C_S evaluations, shown in Figure 5c,d, the untreated sample has lower charge delivered with respect to that accumulated at lower scan rates. Furthermore, the as grown sample showed the lowest coulombic efficiency trend for scan rates lower than 10 mV s^{-1} and lower areal capacitances for scan rates lower than 1 mV s^{-1}. The latter has also been observed for the sample treated at 150 °C, suggesting the presence of catalytic points that get more efficient towards reduction by slowing the rate of the potential sweep, and that for both samples the maximum density of storage is reached around 1 mV s^{-1}. By performing thermal treatments above 150 °C these sites seem to decrease or

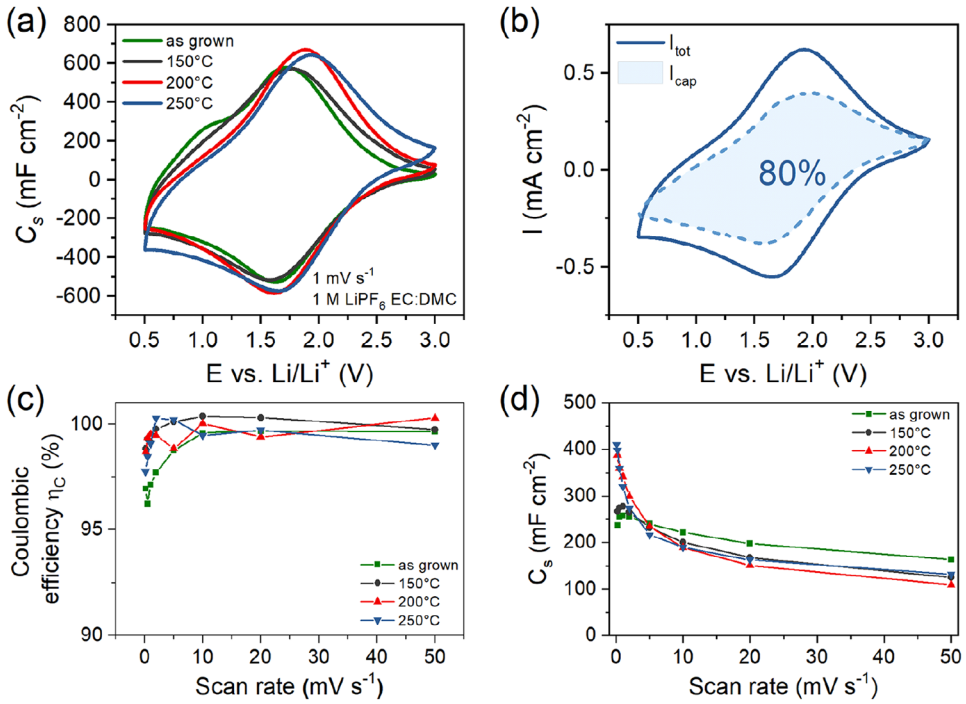

Figure 5. (a) Cyclic voltammograms at 1 mV s^{-1} in organic electrolyte of the amorphous and annealed black TiO_2 NTs samples. As-grown amorphous NTs are displayed in green, whereas the samples annealed at 150 °C, 200 °C, and 250 °C are displayed in black, red, and blue, respectively. (b) Decomposition of the capacitive-controlled current contribution I_{cap} of the voltammogram at 1 mV s^{-1} of the sample annealed at 250 °C. The total current I_{tot} is drawn in full dark blue, while the capacitive-controlled contribution I_{cap} in dashed lighter blue; (c) coulombic efficiency, η_C and (d) areal capacitances, C_S of the samples tested at increasing scan rates. As-grown amorphous NTs are displayed in green, whereas the samples annealed at 150 °C, 200 °C, and 250 °C are displayed in black, red, and blue, respectively.

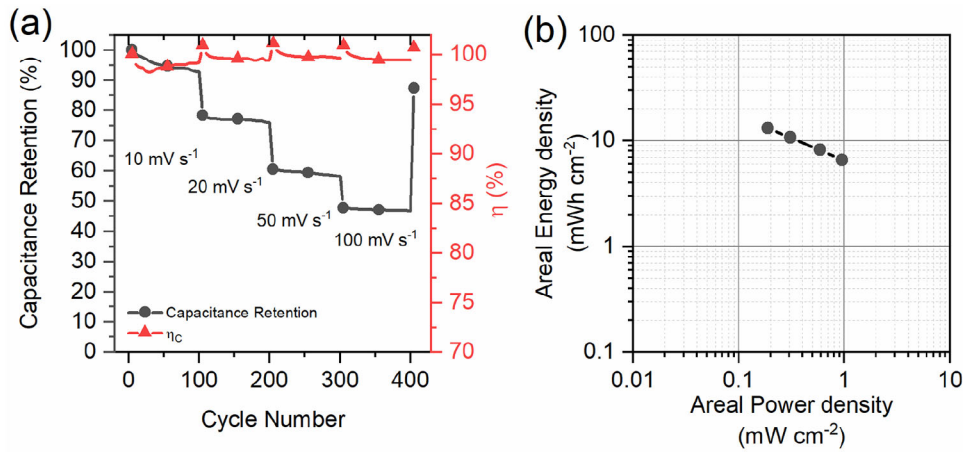

Figure 6. (a) Capacitance retention (in black) and coulombic efficiency η_C (in red) and (b) Ragone plot of the half cell with the NTs annealed at 250 °C.

disappear allowing a better storage efficiency and higher storage capability at slow scan rates, as shown by the calculations performed and the values reported in Table 2.

Based on the results of the capacitive-controlled contribution of charge storage, the cyclability measurements of the electrode treated at 250 °C were performed in half-cell configuration by means of CV tests carried out at scan rates of {10, 20, 50, 100} mV s^{-1}. The results are reported in black in Figure 6a. The areal capacitance is retained above 45% up to 100 mV s^{-1}. Interestingly, the evaluated coulombic efficiencies η_C are fairly high, highlighting the remarkable energy storage properties of these NTs. All values are constantly above 95% as depicted in red in Figure 6a. Finally, the Ragone plot was evaluated to provide information about areal power and energy densities, as can be seen in Figure 6b. As can be seen in Table 3, a comparison was performed in terms of areal capacity, energy and power density between our data and the devices reported in literature closer to ours. The amorphous black titania samples present higher areal capacities than most of the white amorphous samples.

Table 3. Comparison of areal capacity *Q*s, energy density, and power density values.

NT Sample	TiO_2 Phase	Areal Capacity *Q*s [μAh cm^{-2}]	Energy Density [μWh cm^{-2} μm^{-1}]	Power Density [μWh cm^{-2} μm^{-1}]	Refs.
Black TiO_2	Amorphous	44.4 @ 0.1 mV s^{-1}	2.2	200	This work
TiO_2	Amorphous	1500	N.A.	N.A.	[88]
TiO_2	Anatase	1200	N.A.	N.A.	[88]
Ti-Nb alloy	Anatase	20 @ 1.0C	80 @ 1.0C	10 @ 1.0C	[89]
TiO_2	Amorphous	37	N.A.	N.A.	[90]
TiO_2	Anatase	29	N.A.	N.A.	[90]

3. Conclusions

Nanostructured TiO_2 electrodes were fabricated using anodic oxidation in an ethylene glycol-based solution, resulting in the formation of smooth self-ordered nanotubes, as this method offers a precise control over the nanostructure and morphology of the electrodes. Thermal treatments at different temperatures in a hydrogen atmosphere were then employed to improve the performance of the TiO_2 nanotube electrodes. This reducing annealing aimed at enhancing the NTs defectivity and thus their specific capacitance.

The annealing under reducing atmosphere successfully maintained the amorphous nature of the TiO_2 nanotubes, as confirmed by XRD and Raman spectroscopy, which is crucial for maintaining the unique properties of black amorphous TiO_2, including its high surface area and reactivity. Moreover, the thermal treatment also resulted in an increase in donor density and a lowering of the conduction band of the TiO_2 nanotubes, which led to improved electrical conductivity of the electrodes, as evidenced by an increased charge accumulation.

Electrochemical characterizations revealed a significant increase of approximately 20% of the charge accumulated in a fast manner, referred to as capacitive-controlled charge. This indicates improved charge storage capabilities, particularly in response to fast scan rates.

In summary, the combination of assisted anodization to produce nanostructured TiO_2 electrodes and subsequent thermal treatment in hydrogen successfully enhanced the electrode performances. The thermal treatment maintained amorphicity, increased donor density, lowered the conduction band, and significantly improved charge accumulation, particularly under fast charging conditions, thereby demonstrating the effectiveness of the approach for achieving faster and more enduring TiO_2-based electrodes with enhanced electrochemical properties.

4. Experimental Section

4.1. Synthesis

Nanotubes arrays were grown by anodic oxidation on commercial titanium foil substrates (> 99.9%, MTI Corporation) in a two-step process described elsewhere.[61,62] The substrates were precut into interconnected discs of 18 mm of diameter and suitably masked in order to grow the nanotubes only on the front side of the metallic foil. They were then sonicated in deionized water (DIW) for 10 min and etched in HF 1 wt.% (40%, Carlo Erba) and subsequently rinsed in DIW. The anodization process was undertaken at 25 °C in a thermostatic bath under continuous stirring and by using Ti foil as both counter and working electrodes. The EG-based electrolyte was prepared with 0.5 wt.% of ammonium fluoride (>98%, Sigma Aldrich) and 2.5 wt.% of DIW in EG (≥99.5%, Honeywell). A first anodization step of 5 min at 60 V was performed with a constant power generator (GW Instek SPD- 3606) to obtain the tube template. The first layer of nanotubes was then dissolved by ultrasonicating the samples in hydrogen peroxide (Sigma Aldrich). The second anodization step consisting of 15 min at 60 V was then conducted to obtain a compact layer of ordered amorphous nanotubes. After being thoroughly rinsed in DIW, the samples were annealed in a reducing atmosphere (5% H_2 and 95% Ar) at multiple temperatures from 100 °C up to 250 °C for 3.5 h to maintain their amorphous nature.

4.2. Material Characterizations

Morphological characterizations were performed with a field-emission scanning electron microscope (FESEM, Supra 40, ZEISS, Oberkochen, Germany). The samples crystallography was investigated with a Panalytical X'Pert MRD Pro X-ray diffractometer with a Cu-Kα source (λ = 1.541874 Å) in Brag–Brentano configuration with a step size of 0.026 degrees and a scan speed of 200s/step. The diffractograms obtained were then analyzed with the HighScore Plus Software. The Raman spectra were recorded on a Renishaw InVia micro-Raman with an excitation laser of 514 nm of wavelength. The acquisitions were performed at 5% of the nominal power and 20× microscope objective. The chemical composition was investigated through X-ray photoelectron spectroscopy (XPS) by using a PHI 5000 VersaProbe system (Physical Electronics, Inc. (PHI), Chanhassen, MN, USA). Monochromatic Al-Kα (1486.6 eV) was used as X-ray source, and C 1s peak (284.8 eV) was used as reference for the calibration. Wide-energy and high-resolution (HR) XPS spectra were collected and processed using CasaXPS Software (version 2.3.18). HR spectra deconvolution into individual mixed Gaussian–Lorentzian peaks and asymmetric peaks was obtained after Shirley background subtraction and binding energy (BE) calibration. UV–VIS measurements were performed in diffusive reflectance mode on a Lambda 35 (PerkinElmer, Waltham, MA, USA). The band gap was estimated through the Kubelka–Munk equation with both a direct and indirect gap.

Electrochemical characterizations were performed in three-electrode PAT-Cells (EL-CELL GmbH) connected to a Metrohm potentiostat/galvanostat (PGSTAT302N from Metrohm, Utrecht, The Netherlands) with Nova 2.1 software for the acquisitions. All measurements were done in a metallic lithium semicell with an organic lithium hexafluorophosphate based electrolyte ($LiPF_6$ 1 M in EC:DMC

1:1, Solvionic E00350). Cyclic voltammetries were performed over a 2.5 V potential window (0.5–3 V versus Li/Li^+) with scan rates starting from 0.2 mV s^{-1} to 50 mV s^{-1}, from open circuit potential to cathodic voltages. The first three voltammetries at 0.2 mV s^{-1} were carried out to ensure the formation of a stable SEI. Five cycles were performed for each scan rate, the second one is displayed as the most representative one. Mott Schottky impedance measurements were performed in the 1–3 V versus Li/Li^+ potential window with a potential step of 0.1 V at 1 kHz, 5 kHz, and 10 kHz. The flat band potential was obtained as the intersection of the intercepts of the linear curve of each sample at different frequencies, while the donor density was computed from the measurements at 10 kHz. The cycling stability of the device was tested through galvanostatic charge and discharge in coin cells on Arbin BT2000 instrument.

Acknowledgements

The authors would like to thank Dr. Marco Fontana from Politecnico di Torino for the valuable discussions on the XPS data analysis. These results are part of a project that has received funding from the European Research Council (ERC) under the European Union's ERC Starting Grant agreement "CO2CAP" No. 949,916. This work was partially funded by the project "nuovi Concetti, mAteriali e tecnologie per l'iNtegrazione del fotoVoltAico negli edifici e in uno scenario di generazione diffuSa" ("CANVAS"), funded by the Italian Ministry of the Environment and the Energy Security, through the Research Fund for the Italian Electrical System (type-A call, published on G.U.R.I. n. 192 on 18-08-2022). This study was also carried out within the MOST – Sustainable Mobility Center and received funding from the European Union Next-GenerationEU (PIANO NAZIONALE DI RIPRESA E RESILIENZA (PNRR) – MISSIONE 4 COMPONENTE 2, INVESTIMENTO 1.4 – D.D. 1033 17/06/2022, CN00000023). This research work has also been supported also by the "Progetto Orangees " ORgANics for Green Electrochemical Energy Storage – codice CSEAA_00010″ funded by the Italian Government through the MITE (Ministero della Transizione Ecologica) call 2022 "Bandi di gara di tipo A". This article was also partially funded under the National Recovery and Resilience Plan (NRRP), Mission 4 "Education and Research"—Component 2 "From research to business"—Investment 3.1 "Fund for the realization of an integrated system of research and innovation infrastructures"—Call for tender No. n. 3264 of 28/12/2021 of Italian Ministry of Research funded by the European Union—NextGenerationEU—Project code: IR0000027, Concession Decree No. 128 of 21/06/2022 adopted by the Italian Ministry of Research, CUP: B33C22000710006, Project title: iENTRANCE. This work was conducted within the Technologies for Sustainability Flagship of the Istituto Italiano di Tecnologia. This manuscript reflects only the authors' views and opinions, neither the European Union nor the European Commission can be considered responsible for them.

Open access publishing facilitated by Politecnico di Torino, as part of the Wiley-CRUI-CARE agreement.

Conflict of Interests

The authors declare no conflict of interest.

Data Availability Statement

The data that support the findings of this study are available from the corresponding author upon reasonable request.

Keywords: Amorphous materials · Black titania · Energy devices · Nanotubes · Supercapacitors

[1] M. Grohol, C. Veeh, Study on the Critical Raw Materials for the EU 2023 – Final Report, **2023**.
[2] X. Chen, S. S. Mao, *Chem. Rev.* **2007**, *107*, 2891–2959.
[3] L. Liu, X. Chen, *Chem. Rev.* **2014**, *114*, 9890–9918.
[4] Y. Zhang, Z. Jiang, J. Huang, L. Y. Lim, W. Li, J. Deng, D. Gong, Y. Tang, Y. Lai, Z. Chen, *RSC Adv.* **2015**, *5*, 79479–79510.
[5] M. Ge, C. Cao, J. Huang, S. Li, Z. Chen, K. Q. Zhang, S. S. Al-Deyab, Y. Lai, *J. Mater. Chem. A* **2016**, *4*, 6772–6801.
[6] M. Madian, A. Eychmüller, L. Giebeler, *Batteries* **2018**, *4*, 1–36.
[7] H. Kim, M.-Y. Cho, M.-H. Kim, K.-Y. Park, H. Gwon, Y. Lee, K. C. Roh, K. Kang, *Adv. Energy Mater.* **2013**, *3*, 1500–1506.
[8] H. Wang, C. Guan, X. Wang, H. J. Fan, *Small* **2015**, *11*, 1470–1477.
[9] F. Bella, A. B. Muñoz-García, G. Meligrana, A. Lamberti, M. Destro, M. Pavone, C. Gerbaldi, *Nano. Res.* **2017**, *10*, 2891–2903.
[10] A. Sacco, A. Lamberti, S. Bianco, E. Tresso, in *Handbook of Nanoelectrochemistry* **2015**, 1–23.
[11] C. Zhang, H. Yu, Y. Li, Y. Gao, Y. Zhao, W. Song, Z. Shao, B. Yi, *ChemSusChem* **2013**, *6*, 659–666.
[12] A. A. Belak, Y. Wang, A. Van der Ven, *Chem. Mater.* **2012**, *24*, 2894–2898.
[13] C. S. Lewis, Y. R. Li, L. Wang, J. Li, E. A. Stach, K. J. Takeuchi, A. C. Marschilok, E. S. Takeuchi, S. S. Wong, *ACS Sustain. Chem. Eng.* **2016**, *4*, 6299–6312.
[14] Y. Liu, Y. Yang, *J. Nanomater.* **2016**, *2016*, 1–15.
[15] J. A. Yuwono, P. Burr, C. Galvin, A. Lennon, *ACS Appl. Mater. Interfaces* **2021**, *13*, 1791–1806.
[16] S. Ali, P. M. Ismail, M. Khan, A. Dang, S. Ali, A. Zada, F. Raziq, I. Khan, M. S. Khan, M. Ateeq, W. Khan, S. H. Bakhtiar, H. Ali, X. Wu, M. I. A. Shah, A. Vinu, J. Yi, P. Xia, L. Qiao, *Nanoscale* **2024**, *16*, 4352–4377.
[17] C. Lu, X. Cai, X. Liu, D. Tian, B. Li, J. Li, Z. Lou, *J. Mater. Chem. A* **2024**, *6*, 4883–5230.
[18] Z. Cai, X. Hu, Z. Li, H. He, T. Li, H. Yuan, Y. Zhang, B. Tan, J. Wang, *Water Res.* **2022**, *227*, 119341.
[19] Z.-X. Huang, C. Ma, F.-G. Zhang, Q. Cheng, Q.-Y. Liu, Y.-J. Yuan, X. Zhang, *J. Mater. Chem. A* **2023**, *11*, 7488–7497.
[20] P. Roy, S. Berger, P. Schmuki, *Angew. Chem. Int. Ed.* **2011**, *50*, 2904–2939.
[21] A. Lamberti, A. Sacco, S. Bianco, D. Manfredi, M. Armandi, M. Quaglio, E. Tresso, C. F. Pirri, *Sol. Energy* **2013**, *95*, 90–98.
[22] A. Pedico, A. Lamberti, A. Gigot, M. Fontana, F. Bella, P. Rivolo, M. Cocuzza, C. F. Pirri, *ACS Appl. Energy Mater.* **2018**, *1*, 4440–4447.
[23] W. A. Abbas, I. H. Abdullah, B. A. Ali, N. Ahmed, A. M. Mohamed, M. Y. Rezk, N. Ismail, M. A. Mohamed, N. K. Allam, *Nanoscale. Adv.* **2019**, *1*, 2801–2816.
[24] M.-M. Zhang, J.-Y. Chen, H. Li, C.-R. Wang, *Rare Met.* **2021**, *40*, 249–271.
[25] F. Bella, A. B. Muñoz-García, F. Colò, G. Meligrana, A. Lamberti, M. Destro, M. Pavone, C. Gerbaldi, *ACS Omega* **2018**, *3*, 8440–8450.
[26] H.-P. Jen, M.-H. Lin, L.-L. Li, H.-P. Wu, W.-K. Huang, P.-J. Cheng, E. W.-G. Diau, *ACS Appl. Mater. Interfaces* **2013**, *5*, 10098–10104.
[27] A. Lamberti, A. Chiodoni, N. Shahzad, S. Bianco, M. Quaglio, C. F. Pirri, *Sci. Rep.* **2015**, *5*, 7808.
[28] Y. Du, P. Liu, H. Zhang, L. Zou, K. Deng, X. Li, W. Tian, J. Ji, *Adv. Funct. Mater.* **2024**, *34*, 2309830.
[29] M. M. Muzakir, Z. Zainal, H. N. Lim, A. H. Abdullah, N. N. Bahrudin, M. S. M. Ali, *Energies* **2020**, *13*, 2767.
[30] L. Baudino, P. Zaccagnini, N. Garino, M. Serrapede, M. Laurenti, A. Pedico, C. F. Pirri, A. Lamberti, *ChemElectroChem* **2022**, *9*, e202101652.
[31] J. Brumbarov, J. P. Vivek, S. Leonardi, C. Valero-Vidal, E. Portenkirchner, J. Kunze-Liebhäuser, *J. Mater. Chem. A* **2015**, *3*, 16469–16477.
[32] M. Krbal, S. Ng, M. Motola, L. Hromadko, F. Dvorak, V. Prokop, H. Sopha, J. M. Macak, *Appl. Mater. Today* **2019**, *17*, 104–111.
[33] J. Chen, Y. Fu, F. Sun, Z. Hu, X. Wang, T. Zhang, F. Zhang, X. Wu, H. Chen, G. Cheng, R. Zheng, *Chem. Eng. J.* **2020**, *400*, 125784.

[34] V. Augustyn, P. Simon, B. Dunn, *Energy Environ. Sci.* **2014**, *7*, 1597–1614.
[35] M. Soleimani, J. B. Ghasemi, A. Badiei, *Inorg. Chem. Commun.* **2022**, *135*, 109092.
[36] T. S. Rajaraman, S. P. Parikh, V. G. Gandhi, *Chem. Eng. J.* **2020**, *389*, 123918.
[37] S. G. Ullattil, S. B. Narendranath, S. C. Pillai, P. Periyat, *Chem. Eng. J.* **2018**, *343*, 708–736.
[38] X. Chen, L. Liu, F. Huang, *Chem. Soc. Rev.* **2015**, *44*, 1861–1885.
[39] W. Ren, Y. Yan, L. Zeng, Z. Shi, A. Gong, P. Schaaf, D. Wang, J. Zhao, B. Zou, H. Yu, G. Chen, E. M. B. Brown, A. Wu, *Adv. Healthcare Mater.* **2015**, *4*, 1526–1536.
[40] L. Liao, M. Wang, Z. Li, X. Wang, W. Zhou, *Nanomaterials* **2023**, *13*, 468.
[41] B. Wang, S. Shen, S. S. Mao, *J. Mater.* **2017**, *3*, 96–111.
[42] G. Tang, L. Cao, P. Xiao, Y. Zhang, H. Liu, *J. Power Sources* **2017**, *355*, 1–7.
[43] L. Li, Y. Chen, S. Jiao, Z. Fang, X. Liu, Y. Xu, G. Pang, S. Feng, *Mater. Des.* **2016**, *100*, 235–240.
[44] L. Andronic, A. Enesca, *Front. Chem.* **2020**, *8*, 1–8.
[45] X. Liu, G. Zhu, X. Wang, X. Yuan, T. Lin, F. Huang, *Adv. Energy Mater.* **2016**, *6*, 1600452.
[46] A. Sinhamahapatra, J. P. Jeon, J. S. Yu, *Energy Environ. Sci.* **2015**, *8*, 3539–3544.
[47] C. Fan, C. Chen, J. Wang, X. Fu, Z. Ren, G. Qian, Z. Wang, *Sci. Rep.* **2015**, *5*, 1–10.
[48] Z. Wang, C. Yang, T. Lin, H. Yin, P. Chen, D. Wan, F. Xu, F. Huang, J. Lin, X. Xie, M. Jiang, *Adv. Funct. Mater.* **2013**, *23*, 5444–5450.
[49] E. M. Samsudin, S. B. A. Hamid, J. C. Juan, W. J. Basirun, A. E. Kandjani, *Appl. Surf. Sci.* **2015**, *359*, 883–896.
[50] L. Chen, F. He, Y. Huang, Y. Meng, R. Guo, *J. Alloys Compd.* **2016**, *678*, 5–11.
[51] L. Xin, X. Liu, *RSC Adv.* **2015**, *5*, 71547–71550.
[52] A. Touni, X. Liu, X. Kang, P. A. Carvalho, S. Diplas, K. G. Both, S. Sotiropoulos, A. Chatzitakis, *ChemSusChem* **2021**, *14*, 4993–5003.
[53] Z. Li, H. Bian, X. Xiao, J. Shen, C. Zhao, J. Lu, Y. Y. Li, *ACS Appl. Nano. Mater.* **2019**, *2*, 7372–7378.
[54] C. C. Raj, V. Srimurugan, A. Flamina, R. Prasanth, *Mater. Chem. Phys.* **2020**, *248*, 122925.
[55] X. Lu, G. Wang, T. Zhai, M. Yu, J. Gan, Y. Tong, Y. Li, *Nano Lett.* **2012**, *12*, 1690–1696.
[56] M. Plodinec, I. Grčić, M. G. Willinger, A. Hammud, X. Huang, I. Panžić, A. Gajović, *J. Alloys Compd.* **2019**, *776*, 883–896.
[57] M. Motola, M. Čaplovičová, M. Krbal, H. Sopha, G. K. Thirunavukkarasu, M. Gregor, G. Plesch, J. M. Macak, *Electrochim. Acta* **2020**, *331*, 135374.
[58] Y. Yang, M. R. Hoffmann, *Environ. Sci. Technol.* **2016**, *50*, 11888–11894.
[59] K. Carlson, C. Elliott, S. Walker, M. Misra, S. Mohanty, *J. Electrochem. Soc.* **2016**, *163*, H395–H401.
[60] Y. Yang, L. C. Kao, Y. Liu, K. Sun, H. Yu, J. Guo, S. Y. H. Liou, M. R. Hoffmann, *ACS Catal.* **2018**, *8*, 4278–4287.
[61] A. Lamberti, N. Garino, A. Sacco, S. Bianco, A. Chiodoni, C. Gerbaldi, *Electrochim. Acta* **2015**, *151*, 222–229.
[62] A. Lamberti, D. Manfredi, F. Calignano, C. F. Pirri, *Mater. Today Commun.* **2018**, *15*, 165–170.
[63] M. M. Khader, F. M. N. Kheiri, B. E. El-Anadouli, B. G. Ateya, *J. Phys. Chem.* **1993**, *97*, 6074–6077.
[64] X. Chen, L. Liu, P. Y. Yu, S. S. Mao, *Science* **2011**, *331*, 746–750.
[65] O. Frank, M. Zukalova, B. Laskova, J. Kürti, J. Koltai, L. Kavan, *Phys. Chem. Chem. Phys.* **2012**, *14*, 14567.
[66] Y. Luo, A. Benali, L. Shulenburger, J. T. Krogel, O. Heinonen, P. R. C. Kent, *New J. Phys.* **2016**, *18*, 113049.
[67] E. Baudrin, S. Cassaignon, M. Koelsh, J. Jolivet, L. Dupont, J.-M. Tarascon, *Electrochem. Commun.* **2007**, *9*, 337–342.
[68] A. Niilisk, M. Moppel, M. Pärs, I. Sildos, T. Jantson, T. Avarmaa, R. Jaaniso, J. Aarik, *Open Phys.* **2006**, *4*, 105–116.
[69] V. M. Naik, D. Haddad, R. Naik, J. Benci, G. W. Auner, *MRS Proc.* **2002**, *755*, DD1112
[70] X. Jiang, Y. Zhang, J. Jiang, Y. Rong, Y. Wang, Y. Wu, C. Pan, *J. Phys. Chem. C* **2012**, *116*, 22619–22624.
[71] D. Eder, R. Kramer, *Phys. Chem. Chem. Phys.* **2003**, *5*, 1314–1319.
[72] H. Haerudin, S. Bertel, R. Kramer, *J. Chem. Soc. – Faraday Trans.* **1998**, *94*, 1481–1487.
[73] G. Wang, H. Wang, Y. Ling, Y. Tang, X. Yang, R. C. Fitzmorris, C. Wang, J. Z. Zhang, Y. Li, *Nano Lett.* **2011**, *11*, 3026–3033.
[74] A. Naldoni, M. Allieta, S. Santangelo, M. Marelli, F. Fabbri, S. Cappelli, C. L. Bianchi, R. Psaro, S, *J. Am. Chem. Soc.* **2012**, *134*, 7600–7603.
[75] X. Chen, L. Liu, Z. Liu, M. A. Marcus, W.-C. Wang, N. A. Oyler, M. E. Grass, B. Mao, P.-A. Glans, P. Y. Yu, J. Guo, S. S. Mao, *Sci. Rep.* **2013**, *3*, 1510.
[76] Y. Y. Song, H. Hildebrand, P. Schmuki, *Surf. Sci.* **2010**, *604*, 346–353.
[77] L.-B. Mo, Y. Bai, Q.-Y. Xiang, Q. Li, J.-O. Wang, K. Ibrahim, J.-L. Cao, *Appl. Phys. Lett.* **2014**, *105*, 202114.
[78] S. Valencia, J. M. Marin, G. Restrepo, J. M. Marín, G. Restrepo, *Open Mater. Sci. J.* **2010**, *4*, 9–14.
[79] H. H. Pham, L.-W. Wang, *Phys. Chem. Chem. Phys.* **2015**, *17*, 541–550.
[80] K. K. Ghuman, C. V. Singh, *J. Phys. Chem. C* **2016**, *120*, 27910–27916.
[81] Y. Cheng, J. Gao, Q. Shi, Z. Li, W. Huang, *J. Alloys Compd.* **2022**, *901*, 163562.
[82] W. G. Lee, S. I. Woo, J. C. Kim, S. H. Choi, K. H. Oh, *Thin Solid Films* **1994**, *237*, 105–111.
[83] Q. Cheng, W. Ahmad, G. Liu, K. Wang, *Proc. IEEE Conf. Nanotechnol.* **2011**, 1598–1601.
[84] W.-H. Ryu, D.-H. Nam, Y.-S. Ko, R.-H. Kim, H.-S. Kwon, *Electrochim. Acta.* **2012**, *61*, 19–24.
[85] R. Menéndez, P. Alvarez, C. Botas, F. Nacimiento, R. Alcántara, J. L. Tirado, G. F. Ortiz, *J. Power Sources* **2014**, *248*, 886–893.
[86] H. Xiong, H. Yildirim, E. V. Shevchenko, V. B. Prakapenka, B. Koo, M. D. Slater, M. Balasubramanian, S. K. R. S. Sankaranarayanan, J. P. Greeley, S. Tepavcevic, N. M. Dimitrijevic, P. Podsiadlo, C. S. Johnson, T. Rajh, *J. Phys. Chem. C* **2012**, *116*, 3181–3187.
[87] J. Wang, J. Polleux, J. Lim, B. Dunn, *J. Phys. Chem. C* **2007**, *111*, 14925–14931.
[88] W. Cao, K. Chen, D. Xue, *Materials (Basel)* **2021**, *14*, 510.
[89] G. D. Salian, B. M. Koo, C. Lefevre, T. Cottineau, C. Lebouin, A. T. Tesfaye, P. Knauth, V. Keller, T. Djenizian, *Adv. Mater. Technol.* **2018**, *3*, 1700274.
[90] G. F. Ortiz, I. Hanzu, P. Knauth, P. Lavela, J. L. Tirado, T. Djenizian, *Electrochem. Acta* **2009**, *54*, 4262–4268.

Manuscript received: October 02, 2024
Accepted manuscript online: November 18, 2024
Version of record online: ■■, ■■